International Journal of Minerals, Metallurgy and Materials
Volume 27, Number 10, October 2020, Page 1318
https://doi.org/10.1007/s12613-020-2040-1

Effect of Ti content on microstructure and properties of Ti_xZrVNb refractory high-entropy alloys

Tian-dang Huang[1)], *Shi-yu Wu*[1)], *Hui Jiang*[2)], *Yi-ping Lu*[1)], *Tong-min Wang*[1)], *and Ting-ju Li*[1)]

1) Key Laboratory of Solidification Control and Digital Preparation Technology (Liaoning Province), School of Materials Science and Engineering, Dalian University of Technology, Dalian 116024, China

2) College of Mechanical and Electronic Engineering, Shandong University of Science and Technology, Qingdao 266590, China

(Received: 27 December 2019; revised: 29 February 2020; accepted: 6 March 2020)

Abstract: This study aimed to investigate the microstructure and mechanical properties of Ti_xZrVNb (x = 1, 1.5, 2) refractory high-entropy alloys at room and elevated temperatures. The TiZrVNb alloy consisted of the body-centered cubic (bcc) matrix with a small amount of V_2Zr phase. The $Ti_{1.5}ZrVNb$ and Ti_2ZrVNb alloys exhibited a single-phase bcc structure. At room temperature, the tensile ductility of the as-cast alloys increased from 3.5% to 12.3% with the increase in the Ti content. The Ti_xZrVNb alloys exhibited high yield strength at 600°C, and the ultimate yield strength was more than 900 MPa. Softening occurred at 800°C, but the ultimate yield strength could still exceed 200 MPa. Moreover, the Ti_xZrVNb alloys displayed low densities but high specific yield strengths (SYSs). The lowest density of Ti_xZrVNb alloys was only 6.12 g/cm^3, but the SYS could reach about 180 MPa·cm^3·g^{-1}, which is better than those of most reported high-entropy alloys (HEAs).

Keywords: high-entropy alloys; mechanical properties; low density; elevated temperature

1. Introduction

In recent years, a new series of alloys called high-entropy alloys (HEAs) [1] or multi-principal element alloys [2] has become a research focus [3]; this is because of the excellent properties of the alloys, such as high strength [4–5], high ductility [6–7], high-temperature stability [5,8], oxidation resistance [9], wear [10] and corrosion resistance [11], and magnetic properties [12]. Such characteristics have made HEAs potentially valuable in industrial applications [13].

As a branch of HEAs, refractory high-entropy alloys (RHEAs), which are generally composed of refractory elements, such as Ti, Zr, Hf, Nb, V, Ta, Mo, and W [14], have shown potential industrial applications. Some RHEAs exhibit some remarkable properties [15], such as high strength at room temperature [16] and elevated temperature [17–18], low density [19–20], oxidation resistance [21], and radiation resistance [22]. Of these characteristics, the mechanical properties of RHEAs at elevated temperatures are the most remarkable and have made RHEAs replace super alloys in some applications such as turbine and aero-engine blade manufacture [23–27].

Nevertheless, RHEAs also have some disadvantages. Most RHEAs have a body-centred cubic (bcc) structure [13] because most refractory elements are bcc-structured, which generally results in high strength but weak plasticity [28–29], especially at room temperature. The slip systems of a bcc structure are fewer than those of a face-centred cubic (fcc) structure. In addition, although some RHEAs, such as MoNbTaW (13.75 g/cm^3) [30] and TiZrHfNbTa (9.94 g/cm^3) [31], have good mechanical properties, their densities are high. These disadvantages hinder the industrial application of RHEAs.

In this study, a new series of RHEAs, Ti_xZrVNb alloys, with low density and high specific yield strength (SYS) was designed, and the microstructure and mechanical properties at room and elevated temperatures were also studied.

2. Experimental

The purity of the raw materials (Ti, Zr, V, and Nb) was more than 99.99wt%. Vacuum arc melting was used to melt the alloys. The vacuum chamber during the melting process was evacuated to 3×10^{-3} Pa and backfilled to 0.05 Pa with high-purity argon gas. All the alloys were remelted at least six times and solidified in a water-cooled copper hearth to en-

Corresponding author: Yi-ping Lu E-mail: luyiping@dlut.edu.cn

sure homogenization. The crystal structures of the alloys were identified using a Shimadzu 6000 X-ray diffractometer (XRD). The range of the scanning angle (2θ) was 20°–100°, and the scanning speed was 4°/min. The microstructure and phase composition of the alloys were analysed using a JXA-8530F PLUS electron probe microanalyzer (EPMA) equipped with an energy-dispersive X-ray spectrometer (EDS). The transmission electron microscopy (TEM) test was processed using a Tecnai G20 instrument. Vickers hardness was measured using an MH-50 hardness tester under a load of 4.9 N for 15 s. The densities of samples were measured by the Archimedes method using a TOLEDO ME204E accurate electronic balance. The mechanical properties at room temperature were measured using a DNS-100 uniaxial compression tester. The compressive samples were cylindrical (5 mm in diameter and 10 mm in height). The tensile sample was dog bone-shaped, with gauge dimensions of 28 mm in length and 4 mm in width and thickness. The mechanical property at elevated temperature was processed using a Gleeble-3500 thermal simulation machine; the size of the sample was the same as that used for the room-temperature compressive test. The heating rate of the test temperature was 5 K/s, which was maintained for 5 min before the test. The strain rate of all the mechanical property tests was 1×10^{-3} s^{-1}.

3. Results and discussion

Fig. 1 shows the XRD patterns of the Ti_xZrVNb alloys. According to the patterns, all the alloys exhibited a typical single-phase bcc structure. The diffraction peak shifted to a lower angle with the increase in the Ti content, indicating the occurrence of lattice expansion. The values of the lattice constants of TiZrVNb, $Ti_{1.5}ZrVNb$, and Ti_2ZrVNb alloys were 0.3303, 0.3313, and 0.3317 nm, respectively, confirming the expansion of lattice with the increase in the Ti content.

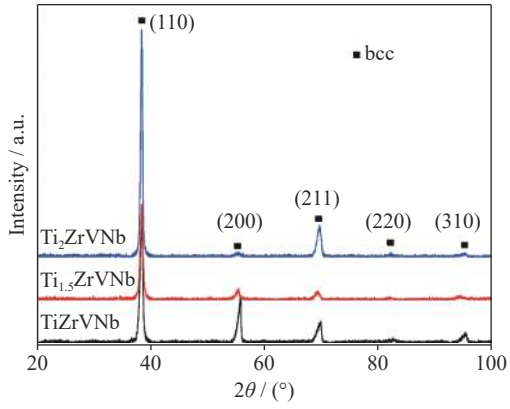

Fig. 1. XRD patterns of Ti_xZrVNb alloys.

Fig. 2 shows the EPMA images of the Ti_xZrVNb alloys. Different from the XRD patterns, a small number of dots and needle-like precipitation phases were observed in the TiZrVNb alloy, and they represent the precipitation phase (about 4.9% in volume fraction), which was too small to be identified by XRD. The EDS results shown in Table 1 indicate that the precipitation phase (denoted by P) was rich in Zr and V. The closer the precipitation phase to the boundary, the larger its size. The solidification of the boundary region occurred later compared with that of the grain, which was beneficial to the growth of the precipitation phase. Composition fluctuation was also observed in the TiZrVNb alloy. Moreover, almost no precipitation phase was observed in the $Ti_{1.5}ZrVNb$ and Ti_2ZrVNb alloys. The composition fluctuations in the $Ti_{1.5}ZrVNb$ and Ti_2ZrVNb alloys were much lower than that of the TiZrVNb alloy because the difference in melting temperature between the dendrite (denoted by D, the dark grey region in Fig. 2) and interdendritic (denoted by ID, the light grey region) region decreased with the increase in the Ti content. As presented in Table 1, the dendrite region was rich in Zr and Nb, and the interdendritic region was rich in V, while Ti was uniformly distributed in the dendrite, interdendrite, and precipitation phase regions. According to the V–Zr binary phase diagram [32], when the atomic ratio of V to Zr was closer to 1:1, the V_2Zr precipitation phase might have formed. According to the calculated isothermal section of the Ti–V–Zr system at different temperatures [33], the increase in the Ti content within a certain range could inhibit the formation of the V_2Zr precipitation phase during the solidification process. Therefore, almost no precipitation phase was observed in the $Ti_{1.5}ZrVNb$ and Ti_2ZrVNb alloys.

Fig. 3 displays the TEM image of the TiZrVNb alloy. In agreement with the EPMA image, the TiZrVNb alloy exhibited a dual-phase structure composed of a matrix and a precipitation phase. According to the analysis of the $[1\bar{1}\bar{2}]$ zone axis (Z) in the selected-area electron diffraction (SAED) image, the precipitation phase was confirmed to be V_2Zr precipitation, which is consistent with previous findings. In addition, an elongated spot was also observed in the SAED image, which indicates stacking fault in the V_2Zr precipitation phase.

Fig. 4 shows the Vickers hardness of the Ti_xZrVNb alloys. The decrease in hardness linearly correlated with the increase in the Ti content. The densities of the Ti_xZrVNb alloys also decreased with the increase in the Ti content. That is, due to the increase in the Ti content, which had the lowest density (4.54 g/cm^3) compared with the densities of the other elements in the Ti_xZrVNb alloy (6.49 g/cm^3 for Zr, 5.96 g/cm^3 for V, and 8.57 g/cm^3 for Nb), the average density of the alloy reduced.

The yield strength $\left(\sigma_{0.2}^{cal}\right)$ of the bcc-structured HEAs prepared by vacuum arc melting could be roughly calculated using Eq. (1) [15]:

$$\sigma_{0.2}^{cal} = \sigma_{0.2}^{mix} + \Delta\sigma \quad (1)$$

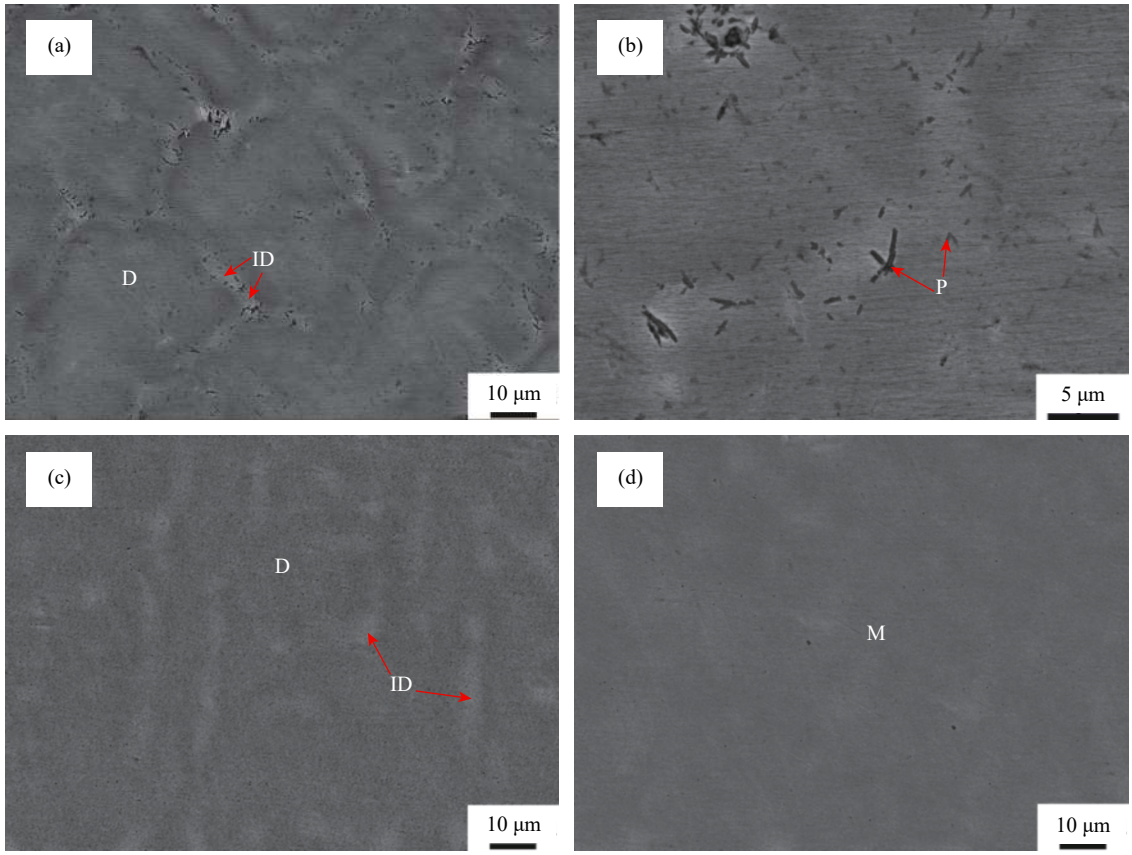

Fig. 2. EPMA images of Ti_xZrVNb alloys: (a) TiZrVNb; (b) TiZrVNb at high magnification; (c) $Ti_{1.5}ZrVNb$; (d) Ti_2ZrVNb (M—Matrix).

Table 1. Chemical compositions of different regions in Fig. 2 for TiZrVNb, $Ti_{1.5}ZrVNb$, and Ti_2ZrVNb alloys at%

Alloy	Region	Ti	Zr	V	Nb
TiZrVNb	D	24.46	35.95	23.61	15.98
	ID	25.26	24.30	28.65	21.79
	P	20.46	33.64	31.91	13.99
$Ti_{1.5}ZrVNb$	D	34.65	18.72	24.02	22.61
	ID	35.11	23.24	22.85	18.80
Ti_2ZrVNb	M	40.59	20.59	20.32	18.50

where $\sigma_{0.2}^{mix}$ is the yield strength calculated using the mixture rule, and $\Delta\sigma$ is the solid solution strengthening (SSS) of the alloy, which can be calculated using Eq. (2):

$$\Delta\sigma = \left(\sum \Delta\sigma_i^{3/2}\right)^{2/3} \quad (2)$$

where $\Delta\sigma_i$ is the SSS caused by the ith element. The parameters required in the calculation were according to those used in previous studies [15,34–35]. The yield strengths of the Ti_xZrVNb alloys calculated by simultaneous Eqs. (1) and (2) were 1381, 1265, and 1116 MPa for TiZrVNb, $Ti_{1.5}ZrVNb$, and Ti_2ZrVNb, respectively. The reduction in lattice distortion and the weakening of SSS due to the decrease in atomic radius difference (4.80%, 4.71%, and 4.61% for TiZrVNb, $Ti_{1.5}ZrVNb$, and Ti_2ZrVNb, respectively) were the main causes of the decrease in yield strength.

Fig. 5 displays the tensile engineering stress–strain curves of the Ti_xZrVNb alloys at room temperature. According to the curves, with the increase in the Ti content, the strength decreased slightly but ductility increased significantly. The yield strength of TiZrVNb (1116 MPa) was greater than that of Ti_2ZrVNb (1058 MPa), by about 5.2%. The ductility of TiZrVNb (3.5%) was less than that of Ti_2ZrVNb (12.3%), by about 251%. The values of density, hardness, and mechanical properties of the Ti_xZrVNb alloys are presented in Table 2.

The trends of the experimental yield strength and the calculated yield strength with the increase in the Ti content were consistent. However, the experimental values were lower than the calculated values. The ratios of the experimental strength to the calculated yield strength were 80.8%, 87.0%, and 94.8% for TiZrVNb, $Ti_{1.5}ZrVNb$, and Ti_2ZrVNb alloys, respectively. The reason for the discrepancy between the cal-

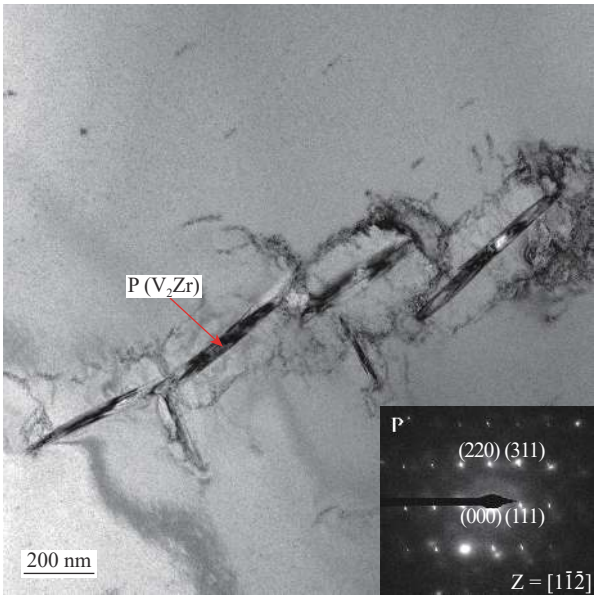

Fig. 3. TEM image of bright field of the TiZrVNb alloy. Inset shows the SAED image of the precipitation phase (P).

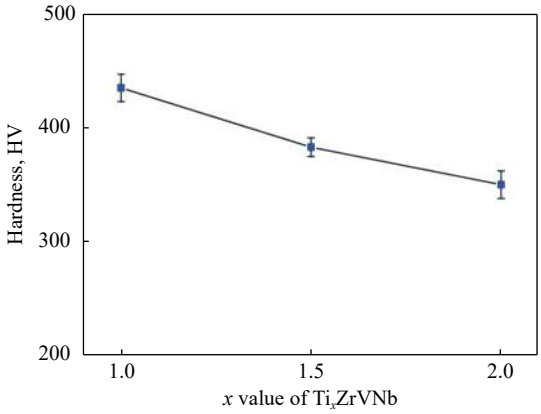

Fig. 4. Vickers hardness of Ti_xZrVNb alloys.

culated and the experimental yield strengths is as follows: TiZrVNb alloy is a dual-phase structure composed of a matrix and a V_2Zr phase; therefore, the aforementioned equation is not completely applicable to the TiZrVNb alloy. For the $Ti_{1.5}ZrVNb$ and Ti_2ZrVNb alloys, the composition fluctuation should be the main reason; therefore, the experimental strength of the Ti_2ZrVNb alloy, which had less composition fluctuation, was closer to the calculated yield strength than that of the $Ti_{1.5}ZrVNb$ alloy. Moreover, the error of the equations also needs to be considered. The improvement in ductility was due to the decrease in stress concentration caused by the disappearance of the needle-like V_2Zr phase and the increase in component uniformity.

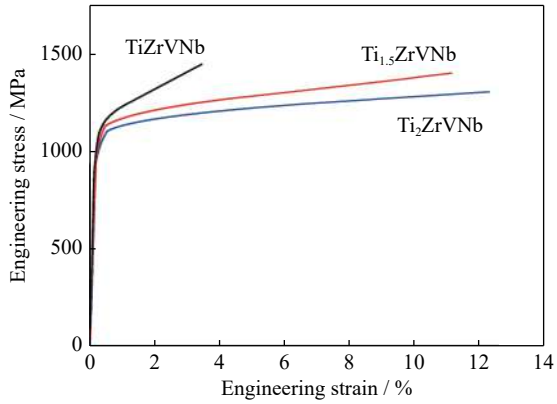

Fig. 5. Tensile engineering stress–strain curves of Ti_xZrVNb alloys at room temperature.

Fig. 6 presents scanning electron microscope (SEM) images of the tensile fracture surfaces of the Ti_xZrVNb alloys at room temperature. Tearing edges and river patterns were observed in the TiZrVNb alloy, indicating that the fracture of the TiZrVNb alloy was quasi-cleavage one. Different from the TiZrVNb alloy, tearing edges, cleavage planes, and dimples were observed in the $Ti_{1.5}ZrVNb$ and Ti_2ZrVNb alloys, indicating that the fractures of the $Ti_{1.5}ZrVNb$ and Ti_2ZrVNb alloys were mixed fractures. Thus, the strength and ductility of the $Ti_{1.5}ZrVNb$ and Ti_2ZrVNb alloys were higher than those of the TiZrVNb alloy. Table 3 presents the EDS results of different regions in the tensile fracture surfaces of the Ti_xZrVNb alloys; the tearing edge regions of the $Ti_{1.5}ZrVNb$ and Ti_2ZrVNb alloys (denoted by B and D) were rich in Zr, indicating that the segregation of the Zr element reduced the ductility. The dimple region was rich in Nb (denoted by C and E), but the segregation degree was lower than that of the Zr element in the tearing edge region.

Table 2. Density, hardness, and mechanical properties of Ti_xZrVNb alloys at room temperature

Alloy	Density / ($g \cdot cm^{-3}$)	Hardness, HV	Tensile yield strength / MPa	Tensile fracture strength / MPa	Tensile ductility / %
TiZrVNb	6.45	434.9	1116	1447	3.5
$Ti_{1.5}ZrVNb$	6.22	383.1	1101	1401	11.2
Ti_2ZrVNb	6.12	350.4	1058	1305	12.3

Fig. 7 displays the compressive engineering stress–strain curves of the TiZrVNb, $Ti_{1.5}ZrVNb$, and Ti_2ZrVNb alloys at room temperature, 600°C, and 800°C. At room temperature, with the increase in the Ti content, the yield strength of TiZrVNb (1229 MPa) was slightly higher than that of Ti_2ZrVNb (1086 MPa), by about 11%. The room temperature compression ratio of the TiZrVNb alloy was about 35.2%, but no fractures occurred in the $Ti_{1.5}ZrVNb$ and Ti_2ZrVNb alloys until compression deformation exceeded 50%. At 600°C, all the Ti_xZrVNb alloys still maintained high strengths, about

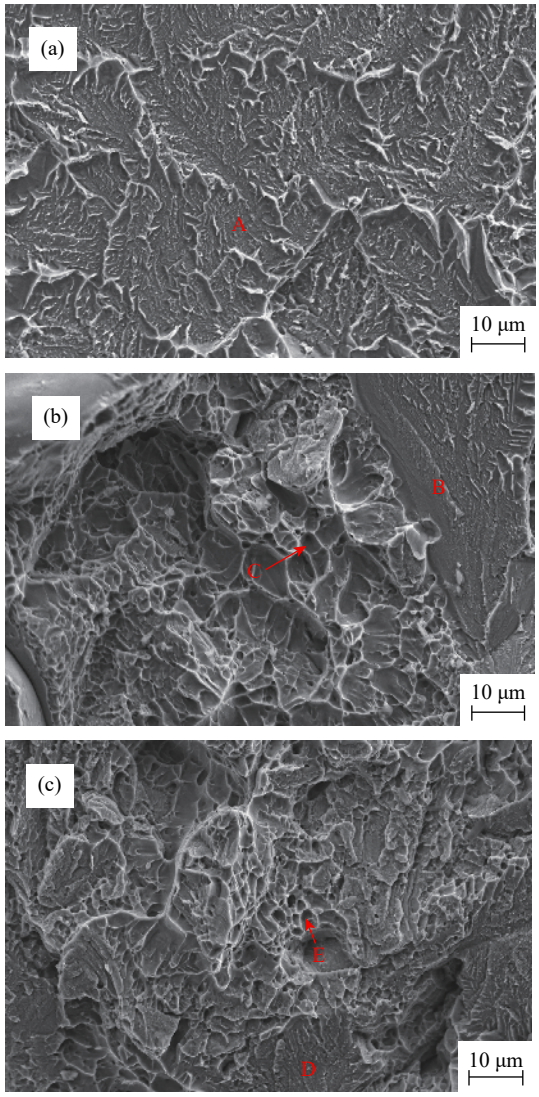

Fig. 6. SEM images of the tensile fracture surfaces of Ti_xZrVNb alloys at room temperature: (a) TiZrVNb; (b) $Ti_{1.5}ZrVNb$; (c) Ti_2ZrVNb.

Table 3. EDS results of the tensile fracture surfaces in Fig. 6 for Ti_xZrVNb alloys at%

Region	Ti	Zr	V	Nb
A	26.63	24.36	23.95	25.05
B	32.91	28.38	19.36	19.35
C	32.42	19.73	21.98	25.87
D	37.31	26.29	19.91	16.49
E	39.63	18.43	18.67	23.27

75% of those at the room temperature. When the temperature was increased to 800°C, the strengths of the Ti_xZrVNb alloys significantly decreased. Moreover, a serrated curve was also observed at 800°C due to the alternating softening deformation and recrystallization. The values of compressive mechanical properties at elevated temperatures are listed in

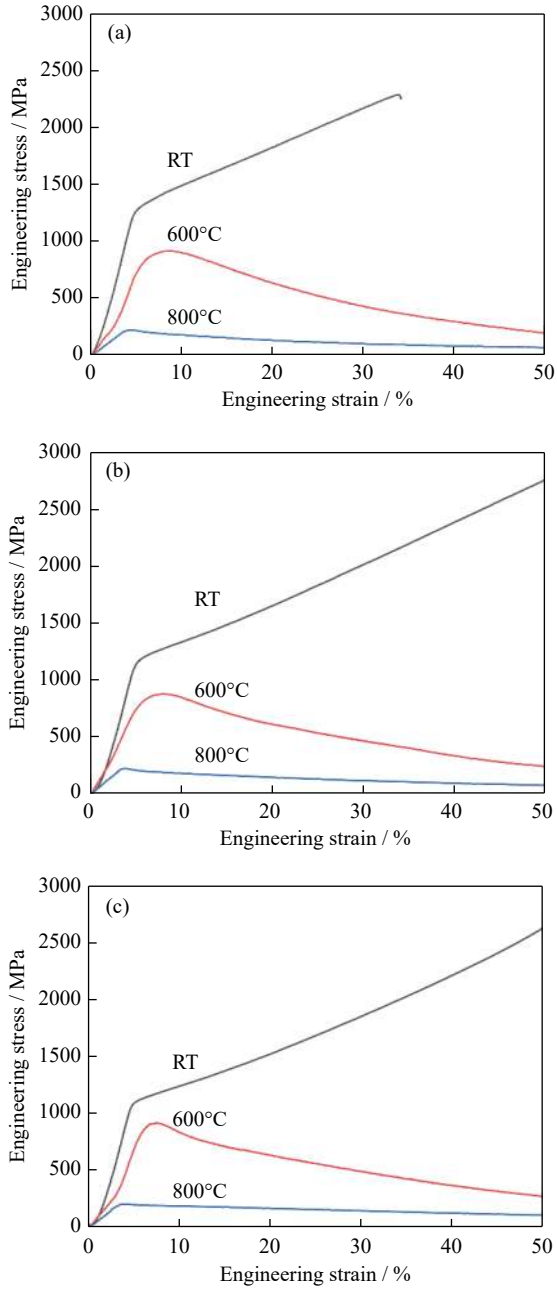

Fig. 7. Compressive engineering stress–strain curves of Ti_xZrVNb alloys at different temperatures: (a) TiZrVNb; (b) $Ti_{1.5}ZrVNb$; (c) Ti_2ZrVNb (RT—Room temperature).

Table 4. The table shows that all the Ti_xZrVNb alloys maintained a high strength until the temperature reached 600°C. The yield strengths of the Ti_xZrVNb alloys with different Ti contents were almost the same at the same temperature, implying that the increase in the Ti content could not change the properties at high temperatures, but improve the ductility at room temperature.

The compressive SYSs and compressive strains of Ti_xZrVNb alloys and some typical HEAs at room temperature [17,19,36–47] are summarized in Fig. 8. Some HEAs with

Table 4. Compressive properties of Ti_xZrVNb alloys at different temperatures

Temperature	Compressive property	TiZrVNb	$Ti_{1.5}ZrVNb$	Ti_2ZrVNb
Room temperature	Yield strength / MPa	1229	1119	1086
	Compressive strength / MPa	2287	—	—
	Compressive ductility / %	35.2	>50	>50
600°C	Yield strength / MPa	768	778	834
	Compressive strength / MPa	923	886	922
	Compressive ductility / %	>50	>50	>50
800°C	Yield strength / MPa	227	233	204
	Compressive strength / MPa	233	236	211
	Compressive ductility / %	>50	>50	>50

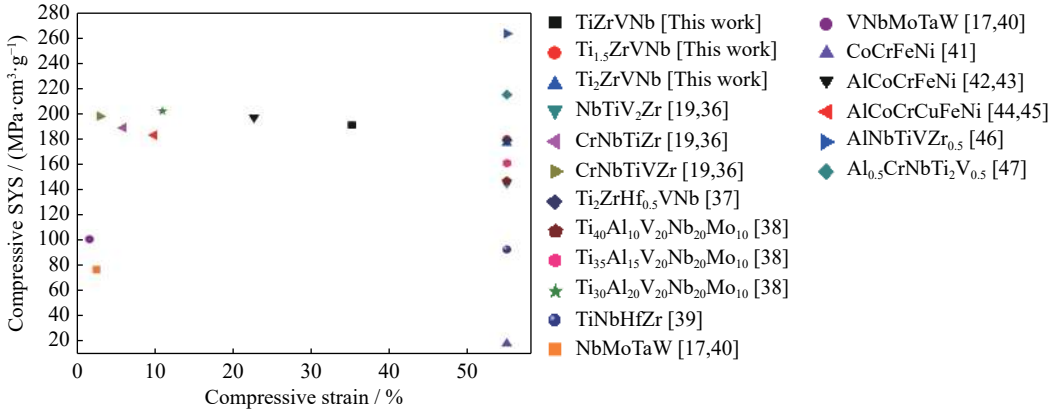

Fig. 8. Compressive SYSs and compressive ductilities of Ti_xZrVNb alloys and some typical HEAs at room temperature.

high SYSs, such as $Ti_{30}Al_{20}V_{20}Nb_{20}Mo_{10}$ and AlCoCrFeNi, had poor compressive ductilities. Some other HEAs with high compressive ductilities, such as CoCrFeNi, had low SYSs because of the high density. Nevertheless, the $Ti_{1.5}ZrVNb$ and Ti_2ZrVNb alloys exhibited good SYSs with high compressive ductilities. Both alloys showed great application potential at room and elevated temperatures. The values of density, compressive SYS, and compressive ductility of the Ti_xZrVNb and typical HEAs listed in Fig. 8 are presented in Table 5.

Table 5. Densities, compressive SYSs, and compressive ductilities of Ti_xZrVNb alloys and some typical HEAs at room temperature

Alloy	Density / ($g \cdot cm^{-3}$)	SYS / ($MPa \cdot cm^3 \cdot g^{-1}$)	Compressive strain /%	Refs.
TiZrVNb	6.45	191	35.2	This work
$Ti_{1.5}ZrVNb$	6.22	180	>50	This work
Ti_2ZrVNb	6.12	177	>50	This work
$NbTiV_2Zr$	6.34	145	>50	[19,36]
CrNbTiZr	6.67	189	6	[19,36]
CrNbTiVZr	6.57	198	3	[19,36]
$Ti_2ZrHf_{0.5}VNb$	6.47	179	>50	[37]
$Ti_{40}Al_{10}V_{20}Nb_{20}Mo_{10}$	6.10	147	>50	[38]
$Ti_{35}Al_{15}V_{20}Nb_{20}Mo_{10}$	6.03	161	>50	[38]
$Ti_{30}Al_{20}V_{20}Nb_{20}Mo_{10}$	5.88	202	11	[38]
TiNbHfZr	9.94	93	>50	[39]
NbMoTaW	13.75	77	2.6	[17,40]
VNbMoTaW	12.36	101	1.7	[17,40]
CoCrFeNi	8.13	19	>50	[41]
AlCoCrFeNi	7.00	197	22.7	[42–43]
AlCoCrCuFeNi	7.10	183	9.9	[44–45]
$AlNbTiVZr_{0.5}$	5.64	263	>50	[46]
$Al_{0.5}CrNbTi_2V_{0.5}$	5.76	215	>50	[47]

4. Conclusions

(1) The TiZrVNb alloy comprised a bcc matrix and a small amount of V_2Zr precipitation phase. The $Ti_{1.5}ZrVNb$ and Ti_2ZrVNb alloys exhibited a single-phase bcc structure. The precipitation phase disappeared with the increase in the Ti content.

(2) At room temperature, the mechanical properties significantly increased with the increase in the Ti content; the tensile ductility of TiZrVNb (3.5%) was less than that of Ti_2ZrVNb (12.3%).

(3) The Ti_xZrVNb alloys exhibited high strength at 600°C; the yield strengths of TiZrVNb, $Ti_{1.5}ZrVNb$, and Ti_2ZrVNb alloys were 923, 886, and 922 MPa, respectively. Softening occurred at 800°C; the yield strengths of TiZrVNb, $Ti_{1.5}ZrVNb$, and Ti_2ZrVNb alloys were 233, 236, and 211 MPa, respectively.

(4) The $Ti_{1.5}ZrVNb$ and Ti_2ZrVNb alloys exhibited good SYSs (180 MPa·cm^3·g^{-1} and 177 MPa·cm^3·g^{-1}, respectively) with high compressive ductilities (>50%) at room temperature. Therefore, both alloys have great application potential.

Acknowledgements

This work was financially supported by the National Magnetic Confinement Fusion Energy R&D Program (No. 2018YFE0312400), the National Natural Science Foundation of China (Nos. 51822402 and 51671044), the National Key Research and Development Program of China (Nos. 019YFA0209901 and 2018YFA0702901), the Fund of the State Key Laboratory of Solidification Processing in Northwestern Polytechnical University (Grant No. SKLSP201902), the Liaoning Revitalization Talents Program (No. XLYC1807047), and the Fund of Science and Technology on Reactor Fuel and Materials Laboratory (No. STRFML-2020-04).

References

[1] J.-W. Yeh, S.-K. Chen, S.-J. Lin, J.-Y. Gan, T.-S. Chin, T.-T. Shun, C.-H. Tsau, and S.-Y. Chang, Nanostructured high-entropy alloys with multiple principal elements: Novel alloy design concepts and outcomes, *Adv. Eng. Mater.*, 6(2004), No. 5, p. 299.

[2] B. Cantor, I.T.H. Chang, P. Knight, and A.J.B. Vincent, Microstructural development in equiatomic multicomponent alloys, *Mater. Sci. Eng. A*, 375-377(2004), p. 213.

[3] M.C. Gao, J.W. Yeh, P.K. Liaw, and Y. Zhang, *High-Entropy Alloys: Fundamentals and Applications*, Springer International Publishing, Cham, Switzerland, 2016.

[4] O.N. Senkov, J.K. Jensen, A.L. Pilchak, D.B. Miracle, and H.L. Fraser, Compositional variation effects on the microstructure and properties of a refractory high-entropy superalloy $AlMo_{0.5}NbTa_{0.5}TiZr$, *Mater. Des.*, 139(2018), p. 498.

[5] B. Schuh, F. Mendez-Martin, B. Völker, E.P. George, H. Clemens, R. Pippan, and A. Hohenwarter, Mechanical properties, microstructure and thermal stability of a nanocrystalline CoCrFeMnNi high-entropy alloy after severe plastic deformation, *Acta Mater.*, 96(2015), p. 258.

[6] X.Z. Gao, Y.P. Lu, B. Zhang, N.N. Liang, G.Z. Wu, G. Sha, J.Z. Liu, and Y.H. Zhao, Microstructural origins of high strength and high ductility in an $AlCoCrFeNi_{2.1}$ eutectic high-entropy alloy, *Acta Mater.*, 141(2017), p. 59.

[7] S.G. Ma, S.F. Zhang, J.W. Qiao, Z.H. Wang, M.C. Gao, Z.M. Jiao, H.J. Yang, and Y. Zhang, Superior high tensile elongation of a single-crystal $CoCrFeNiAl_{0.3}$ high-entropy alloy by Bridgman solidification, *Intermetallics*, 54(2014), p. 104.

[8] M. Vaidya, K. Guruvidyathri, and B.S. Murty, Phase formation and thermal stability of CoCrFeNi and CoCrFeMnNi equiatomic high entropy alloys, *J. Alloys Compd.*, 774(2019), p. 856.

[9] Z.Y. Rao, X. Wang, Q.J. Wang, T. Liu, X.H. Chen, L. Wang, and X.D. Hui, Microstructure, mechanical properties, and oxidation behavior of $Al_xCr_{0.4}CuFe_{0.4}MnNi$ high entropy alloys, *Adv. Eng. Mater.*, 19(2017), No. 5, art. No. 1600726.

[10] M.H. Chuang, M.H. Tsai, W.R. Wang, S.J. Lin, and J.W. Yeh, Microstructure and wear behaviour of $Al_xCo_{1.5}CrFeNi_{1.5}Ti_y$ high-entropy alloys, *Acta Mater.*, 59(2011), No. 16, p. 6308.

[11] C.Y. Shang, E. Axinte, J. Sun, X.T. Li, P. Li, J.W. Du, P.C. Qiao, and Y. Wang, $CoCrFeNi(W_{1-x}Mo_x)$ high-entropy alloy coatings with excellent mechanical properties and corrosion resistance prepared by mechanical alloying and hot pressing sintering, *Mater. Des.*, 117(2017), p. 193.

[12] T.T. Zuo, S.B. Ren, P.K. Liaw, and Y. Zhang, Processing effects on the magnetic and mechanical properties of $FeCoNiAl_{0.2}Si_{0.2}$ high entropy alloy, *Int. J. Miner. Metall. Mater.*, 20(2013), No. 6, p. 549.

[13] D.B. Miracle and O.N. Senkov, A critical review of high entropy alloys and related concepts, *Acta Mater.*, 122(2017), p. 448.

[14] M.C. Gao, C.S. Carney, Ö.N. Doğan, P.D. Jablonksi, J.A. Hawk, and D.E. Alman, Design of refractory high-entropy alloys, *JOM*, 67(2015), No. 11, p. 2653.

[15] H.W. Yao, J.W. Qiao, J.A. Hawk, H.F. Zhou, M.W. Chen, and M.C. Gao, Mechanical properties of refractory high-entropy alloys: Experiments and modeling, *J. Alloys Compd.*, 696(2017), p. 1139.

[16] Y.D. Wu, Y.H. Cai, T. Wang, J.J. Si, J. Zhu, Y.D. Wang, and X.D. Hui, A refractory $Hf_{25}Nb_{25}Ti_{25}Zr_{25}$ high-entropy alloy with excellent structural stability and tensile properties, *Mater. Lett.*, 130(2014), p. 277.

[17] O.N. Senkov, G.B. Wilks, J.M. Scott, and D.B. Miracle, Mechanical properties of $Nb_{25}Mo_{25}Ta_{25}W_{25}$ and $V_{20}Nb_{20}Mo_{20}Ta_{20}W_{20}$ refractory high entropy alloys, *Intermetallics*, 19(2011), No. 5, p. 698.

[18] H. Chen, A. Kauffmann, B. Gorr, D. Schliephake, C. Seemüller, J.N. Wagner, H.-J. Christ, and M. Heilmaier, Microstructure and mechanical properties at elevated temperatures of a new Al-containing refractory high-entropy alloy Nb–Mo–Cr–Ti–Al, *J. Alloys Compd.*, 661(2016), p. 206.

[19] O.N. Senkov, S.V. Senkova, D.B. Miracle, and C. Woodward, Mechanical properties of low-density, refractory multi-principal element alloys of the Cr–Nb–Ti–V–Zr system, *Mater. Sci. Eng. A*, 565(2013), p. 51.

[20] N.D. Stepanov, D.G. Shaysultanov, G.A. Salishchev, and M.A. Tikhonovsky, Structure and mechanical properties of a lightweight AlNbTiV high entropy alloy, *Mater. Lett.*, 142(2015), p. 153.

[21] C.H. Chang, M.S. Titus, and J.W. Yeh, Oxidation behavior

between 700 and 1300°C of refractory TiZrNbHfTa high-entropy alloys containing aluminum, *Adv. Eng. Mater.*, 20(2018), No. 6, art. No. 1700948.

[22] Y.P. Lu, H.F. Huang, X.Z. Gao, C.L. Ren, J. Gao, H.Z. Zhang, S.J. Zheng, Q.Q. Jin, Y.H. Zhao, C.Y. Lu, T.M. Wang, and T.J. Li, A promising new class of irradiation tolerant materials: $Ti_2ZrHfV_{0.5}Mo_{0.2}$ high-entropy alloy, *J. Mater. Sci. Technol.*, 35(2019), No. 3, p. 369.

[23] O.N. Senkov, S. Rao, K.J. Chaput, and C. Woodward, Compositional effect on microstructure and properties of NbTiZr-based complex concentrated alloys, *Acta Mater.*, 151(2018), p. 201.

[24] H. Chen, A. Kauffmann, S. Seils, T. Boll, C.H. Liebscher, I. Harding, K.S. Kumar, D.V. Szabó, S. Schlabach, S. Kauffmann-Weiss, F. Müller, B. Gorr, H.-J. Christ, and M. Heilmaier, Crystallographic ordering in a series of Al-containing refractory high entropy alloys Ta–Nb–Mo–Cr–Ti–Al, *Acta Mater.*, 176(2019), p. 123.

[25] O.N. Senkov, D.B. Miracle, K.J. Chaput, and J.P. Couzinie, Development and exploration of refractory high entropy alloys—A review, *J. Mater. Res.*, 33(2018), No. 19, p. 3092.

[26] N.Y. Yurchenko, N.D. Stepanov, A.O. Gridneva, M.V. Mishunin, G.A. Salishchev, and S.V. Zherebtsov, Effect of Cr and Zr on phase stability of refractory Al–Cr–Nb–Ti–V–Zr high-entropy alloys, *J. Alloys Compd.*, 757(2018), p. 403.

[27] N.Y. Yurchenko, N.D. Stepanov, S.V. Zherebtsov, M.A. Tikhonovsky, and G.A. Salishchev, Structure and mechanical properties of B2 ordered refractory $AlNbTiVZr_x$ (x = 0–1.5) high-entropy alloys, *Mater. Sci. Eng. A*, 704(2017), p. 82.

[28] S.P. Wang and J. Xu, (TiZrNbTa)–Mo high-entropy alloys: Dependence of microstructure and mechanical properties on Mo concentration and modelling of solid solution strengthening, *Intermetallics*, 95(2018), p. 59.

[29] J. Chen, X.Y. Zhou, W.L. Wang, B. Liu, Y.K. Lv, W. Yang, D.P. Xu, and Y. Liu, A review on fundamental of high entropy alloys with promising high-temperature properties, *J. Alloys Compd.*, 760(2018), p. 15.

[30] Y. Zou, P. Okle, H. Yu, T. Sumigawa, T. Kitamura, S. Maiti, W. Steurer, and R. Spolenak, Fracture properties of a refractory high-entropy alloy: *In situ* micro-cantilever and atom probe tomography studies, *Scripta Mater.*, 128(2017), p. 95.

[31] K.R. Lim, K.S. Lee, J.S. Lee, J.Y. Kim, H.J. Chang, and Y.S. Na, Dual-phase high-entropy alloys for high-temperature structural applications, *J. Alloys Compd.*, 728(2017), p. 1235.

[32] N.P. Lyakishev, ed., *Phase Diagrams of Binary Metal Systems*: *A Handbook*, Q.W. Guo, trans., Chemical Industry Press, Beijing, 2009.

[33] J.X. Cui, C.P. Guo, L. Zou, C.R. Li, and Z.M. Du, Experimental investigation and thermodynamic modeling of the Ti–V–Zr system, *Calphad*, 55(2016), p. 189.

[34] W. Martienssen and H. Warlimont, *Springer Handbook of Condensed Matter and Materials Data*, Springer Berlin Heidelberg, New York, 2005.

[35] *Matweb Material Property Data* [2020-07-18]. http://www.matweb.com/

[36] O.N. Senkov, S.V. Senkova, C. Woodward, and D.B. Miracle, Low-density, refractory multi-principal element alloys of the Cr–Nb–Ti–V–Zr system: Microstructure and phase analysis, *Acta Mater.*, 61(2013), No. 5, p. 1545.

[37] D.X. Qiao, H. Jiang, W.N. Jiao, Y.P. Lu, Z.Q. Cao, and T.J. Li, A novel series of refractory high-entropy alloys $Ti_2ZrHf_{0.5}VNb_x$ with high specific yield strength and good ductility, *Acta Metall. Sinica*, 32(2019), No. 8, p. 925.

[38] Z.Q. Xu, Z.L. Ma, M. Wang, Y.W. Chen, Y.D. Tan, and X.W. Cheng, Design of novel low-density refractory high entropy alloys for high-temperature applications, *Mater. Sci. Eng. A*, 755(2019), p. 318.

[39] O.N. Senkov, J.M. Scott, S.V. Senkova, F. Meisenkothen, D.B. Miracle, and C.F. Woodward, Microstructure and elevated temperature properties of a refractory TaNbHfZrTi alloy, *J. Mater. Sci.*, 47(2012), No. 9, p. 4062.

[40] O.N. Senkov, G.B. Wilks, D.B. Miracle, C.P. Chuang, and P.K. Liaw, Refractory high-entropy alloys, *Intermetallics*, 18(2010), No. 9, p. 1758.

[41] T.D. Huang, L. Jiang, C.L. Zhang, H. Jiang, Y.P. Lu, and T.J. Li, Effect of carbon addition on the microstructure and mechanical properties of CoCrFeNi high entropy alloy, *Sci. China, Technol. Sci.*, 61(2018), p. 117.

[42] Z. Tang, O.N. Senkov, C.M. Parish, C. Zhang, F. Zhang, L.J. Santodonato, G.Y. Wang, G.F. Zhao, F.Q. Yang, and P.K. Liaw, Tensile ductility of an AlCoCrFeNi multi-phase high-entropy alloy through hot isostatic pressing (HIP) and homogenisation, *Mater. Sci. Eng. A*, 647(2015), p. 229.

[43] Y. Dong, K.Y. Zhou, Y.P. Lu, X.X. Gao, T.M. Wang, and T.J. Li, Effect of vanadium addition on the microstructure and properties of AlCoCrFeNi high entropy alloy, *Mater. Des.*, 57(2014), p. 67.

[44] A.V. Kuznetsov, D.G. Shaysultanov, N.D. Stepanov, G.A. Salishchev, and O.N. Senkov, Tensile properties of an AlCrCuNiFeCo high-entropy alloy in as-cast and wrought conditions, *Mater. Sci. Eng. A*, 533(2012), p. 107.

[45] J.M. Zhu, H.F. Zhang, H.M. Fu, A.M. Wang, H. Li, and Z.Q. Hu, Microstructures and compressive properties of multicomponent $AlCoCrCuFeNiMo_x$ alloys, *J. Alloys Compd.*, 497(2010), No. 1-2, p. 52.

[46] N.D. Stepanov, N.Y. Yurchenko, V.S. Sokolovsky, M.A. Tikhonovsky, and G.A. Salishchev, An $AlNbTiVZr_{0.5}$ high-entropy alloy combining high specific strength and good ductility, *Mater. Lett.*, 161(2015), p. 136.

[47] N.D. Stepanov, N.Y. Yurchenko, E.S. Panina, M.A. Tikhonovsky, and S.V. Zherebtsov, Precipitation-strengthened refractory $Al_{0.5}CrNbTi_2V_{0.5}$ high entropy alloy, *Mater. Lett.*, 188(2017), p. 162.